Electroosmosis with Step Changes in Zeta Potential in Microchannels

Keisuke Horiuchi
School of Mechanical and Materials Engineering, Washington State University, Pullman, WA 99164
Mechanical Engineering Research Laboratory, Hitachi, Ltd., 832-2 Horiguchi, Hitachinaka, Ibaraki 312-0034, Japan

Prashanta Dutta
School of Mechanical and Materials Engineering, Washington State University, Pullman, WA 99164

Cornelius F. Ivory
School of Chemical Engineering and Bioengineering, Washington State University, Pullman, WA 99164

DOI 10.1002/aic.11275
Published online August 31, 2007 in Wiley InterScience (www.interscience.wiley.com).

This article presents an analytical solution for two-dimensional fluid flow in a rectangular microchannel in the vicinity of a step change in the zeta (ζ) potential. The stream function is determined from the creeping flow approximation to the Navier-Stokes equations assuming a fixed volumetric axial flow, a constant electric field, and thin symmetric double layers. The resulting biharmonic equation is solved using a double-sided Laplace transformation, which is then inverted by Heaviside expansion. The resulting series solution provides closed-form expressions for the velocity and pressure fields that help explain how the recirculating flows generated by an abrupt change in the surface potential may contribute both locally and globally to the hydrodynamic dispersion in straight microchannels. © 2007 American Institute of Chemical Engineers *AIChE J,* 53: 2521–2533, 2007
Keywords: microchannel, electroosmosis, zeta potential, biharmonic equation

Introduction

Very high pressure gradients are needed to drive fluid flows through capillaries and microchannels because of the friction caused by shear stress.[1] Thus, electrokinetic (EK) phenomena such as electroosmosis, streaming potential, electrophoresis, etc., have recently been receiving more attention as effective methods of fluid and chemical transport in microchannels. Electroosmosis and electrophoresis are the most popular EK phenomena because they enjoy a number of practical applications in molecular biology and medical science, such as the separation of deoxyribonucleic acids (DNAs), nucleic acids, viruses, small organelles, and proteins. Over the last 15 years, capillaries have mainly been used for electrophoretic methods because of their high separation efficiencies and peak capacities. More recently, microchannels have attracted the attention of researchers because they are less expensive, simpler to fabricate, and more amenable to integration than capillaries.

In 1879, Helmholtz developed an analytical model for electroosmotic flow (EOF); Smoluchowski expanded upon Helmholtz's attempts in seeking to derive a formula for the electroosmotic velocity in 1921. According to their analysis,

Correspondence concerning this article should be addressed to P. Dutta at dutta@mail.wsu.edu.

a plug-like velocity profile is expected and its amplitude is linearly proportional to both the zeta potential (ζ) and the electric field. This is true when the externally-applied electric field is uniform and both the ζ-potential and channel cross section are constant.

For electrophoresis, some researchers attempted to uniformly suppress EOF[2,3] while others took advantage of the EOF[4,5] to improve performance. In either case, the surface should be electrokinetically homogeneous in order to avoid convective sample dispersion, which lowers separation efficiency. In practice, it is not easy to maintain a homogeneous surface with a uniform ζ-potential. Therefore, a deeper and more comprehensive understanding of the effects of the surface inhomogeneities on peak broadening is required. Some experimental work has shown that polymeric materials, e.g., poly-di-methyl-siloxane (PDMS), develop inhomogeneous surface charges or ζ-potentials.[6,7] Also, variation of the solution pH along the channel strongly affects the ζ-potential distribution[8–10] and, hence, the EOF. The first theoretical treatment of nonuniform ζ-potential on EOF was performed within capillaries.[11] The authors observed that the velocity of the EOF depends primarily on the distribution of the ζ-potential along the wall which, in turn, can either cause flow separation or circulation. Extensions of this work to shallow rectangular channels with wavy surface potential distributions[12] and spot defects[13] were undertaken 10 years later. In those experimental studies, they found recirculating flows which could be useful in the design of microfluidic mixers. Experimental work by Stroock et al.,[14] verified the existence of patterning EOF in both longitudinal and transverse directions. In that study, polyethylene glycol was utilized to reduce the local surface charge of organic polymers. Later, Qian and Bau[15] demonstrated a time-dependent EOF with nonuniform ζ-potential. However, all of the theoretical models mentioned above are limited to spatially periodic boundary conditions.

Herr et al.,[16] addressed the effect of step changes in ζ-potential in capillaries for which both analytical and experimental results indicate the presence of induced pressure gradients and associated band broadening. Dutta et al.,[17] numerically evaluated the performance of a micropump by sandwiching one type of material between another type of material with different values of ζ-potential. Later, Brotherton and Davis[18] showed that sudden changes in either ζ-potential or cross section would cause distortion of the plug-like velocity profile. In those cases they solved for the velocity distribution only in the hydraulically fully-developed region, but did not attempt to calculate the velocity distribution occurring in or near the region of step change.

In addition to above theoretical studies, there are several numerical works on nonuniform ζ-potential.[19–23] Most of these studies consider mixing phenomena in microchannel using nonuniform ζ-potential. This article presents an analysis of the effects of a step change in ζ-potential on flow in a two-dimensional straight microchannel. Such a step change might occur when an oxidative surface modification is carried out inhomogeneously, for example, by masking parts of the surface.[14] A step change may also be caused by adsorption of particles to specific regions on the channel wall.[16] The velocity and pressure distributions near the step change are determined from the Navier-Stokes equations by first solving for the fully-developed velocities far upstream and downstream from the step, and then subtracting the upstream velocity profile from the general expression for the velocity. In this study, the continuity equation is eliminated by substituting the stream function, and the pressure is eliminated by taking the curl of the conservation equation. The resulting biharmonic partial differential equation (PDE) is reduced to a fourth-order ordinary differential equation (ODE) in the transverse coordinate by application of the two-sided Laplace transformation technique. The appropriate no-slip conditions are applied to the solution of this ODE which, in turn, is inverted by using a Heaviside expansion. This solution in terms of the stream function is then used to predict the velocity and pressure fields near the step change.

Analytical versus numerical solutions

Virtually any differential equation that can be solved using analytical techniques can also be solved by numerical methods. In fact, analytical solutions are largely limited to a subset of linear equations on domains which admit conformal boundary conditions whereas numerical methods can readily be brought to bear against nonlinear problems on complex geometries. The increased power and speed of new computers coupled with the availability of commercial simulation packages when weighed against the degree of difficulty of deriving analytical solutions raises the question as to whether analytical solutions should be considered obsolete.

While that day may arrive sooner than we expect, there are several reasons in general why analytical solution are useful and some of these are specific to the problem at hand. First, the analytical solution in this article provides an asymptotic benchmark against which numerical algorithms can be tested. In particular, the discontinuity at $x = 0$ gives rise to deep depressions in the pressure whose centers are located near the velocity discontinuities on the wall. Analytical techniques can rigorously determine whether these depressions are singularities; numerical techniques cannot.

Second, the positive and negative eigenvalues should be identical in both the numerical and analytical solutions and, since the eigenvalues of the analytical solution are expected to be exact, they provide a rigorous test of numerical algorithms, albeit, only in the linear limit and only in conformal geometries. Finally, while analytical solutions handle infinite domains with relative ease, this can be a problem for numerical solutions, especially when the aspect ratio of the geometric axes is very large, as it is in this case.

On this same note, the reader should be aware that singular perturbation methods can provide an important complement to numerical solutions since the accuracy of the perturbation methods generally improves as the small perturbation parameter vanishes while the accuracy of numerical solutions generally degrades in that limit.

Mathematical Model

Consider two parallel plates confining an electrolyte solution as a model of our microchannel. Figure 1 defines the origin of our coordinate system as well as the channel half height, H, and illustrates the "far-field" velocity profiles, $V_{x\infty}$, far upstream and downstream from the origin. The

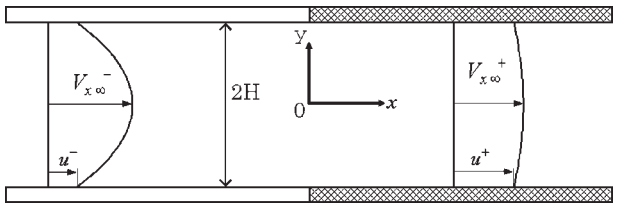

Figure 1. Schematic view of mixed electroosmotic and pressure driven flow with different values of the ζ-potential between upstream ($x < 0$) and downstream ($x \geq 0$) regions.

superscripts, "−" and "+", indicate whether the variables are upstream ($x < 0$) or downstream ($x \geq 0$), respectively. The axial step change in the ζ-potential occurs at the position, $x = 0$, and causes a perturbation in the otherwise straight streamlines as illustrated in Figure 1. Our goal is to find both the velocity and the pressure distribution throughout the channel, focusing especially in the region situated near the step change in ζ-potential at $x = 0$.

Governing equations and boundary conditions

If a uniform electric field, $\vec{E}$, is applied in the axial direction throughout the microchannel, the electrolyte in that channel experiences an electric body force per unit volume, $\rho_e\vec{E}$, because of the Lorentz force, where ρ_e is the net charge density. However, this electrical body force is active only within the Debye layer. If the Debye layer is infinitesimal compared to the channel depth, then it is possible to approximate the steady-state Navier-Stokes equations for incompressible, creeping flow, i.e., $\mathrm{Re} \ll 1$, as

$$\nabla \cdot \vec{V} = 0 \tag{1a}$$

$$-\nabla P + \eta\nabla^2\vec{V} = 0 \tag{1b}$$

with replacement of the no-slip boundary conditions by implicit-slip boundary conditions,[11]

$$\vec{V} = \mu_{eo}\vec{E} = -\frac{\varepsilon\zeta}{\eta}\vec{E} \tag{2}$$

where μ_{eo} is the electroosmotic mobility, ε is the dielectric constant, ζ is the zeta potential, and η is constant dynamic viscosity coefficient. Here the ζ-potential is a function of axial position. This implies that a step change in ζ-potential is identical to the sudden change in EOF velocity along the channel wall. Note that the thin electric double layer (EDL) approximation is valid if the electrolyte ionic concentration is high enough, e.g., if univalent electrolytes have concentrations greater than ~1 mol/m^3 so that the EDL is significantly smaller than the typical channel depth of ~10 μm.

Taking the curl and then the divergence of the momentum Eq. 1b to eliminate the pressure and then the velocity, we find that both velocity and pressure satisfy the Laplace equation which becomes a biharmonic equation in terms of the stream-function vector,[24] $\vec{\Psi} = \begin{bmatrix} 0 & 0 & \psi \end{bmatrix}^T$, as

$$\nabla^2\vec{\Omega} = -\nabla^4\vec{\Psi} = \frac{\partial^4\psi}{\partial x^4} + 2\frac{\partial^4\psi}{\partial x^2\partial y^2} + \frac{\partial^4\psi}{\partial y^4} = L^4(\psi) = L^2(L^2\psi) = 0 \tag{3}$$

where the linear operator, L^2, is defined as $L^2 = \partial^2/\partial x^2 + \partial^2/\partial y^2$. Equation 3 is a fourth-order PDE so it requires four boundary conditions in y and four in x. In this study, the electric field is continuous and one-dimensional, i.e., $\vec{E} = E\,\hat{e}_x$, because the channel length and width are infinitely long relative to the channel height and because electrostatic coupling of the electrolyte ions in the bulk solution has been ignored. With this in mind, the boundary conditions for the stream function are:

$$V_y\big|_{y=\pm H} = -\left.\frac{\partial\psi}{\partial x}\right|_{y=\pm H} = 0 \quad \text{for all x} \tag{4a}$$

$$V_x^+\big|_{y=\pm H} = \left.\frac{\partial\psi^+}{\partial y}\right|_{y=\pm H} = -\frac{\varepsilon\zeta^+}{\eta}E \equiv u^+ \quad \text{for } x \geq 0 \tag{4b}$$

$$V_x^-\big|_{y=\pm H} = \left.\frac{\partial\psi^-}{\partial y}\right|_{y=\pm H} = -\frac{\varepsilon\zeta^-}{\eta}E \equiv u^- \quad \text{for } x < 0 \tag{4c}$$

where, for the purposes of this article, the electroosmotic surface velocities are assumed to be the same on both y-surfaces.

Assumptions

First of all, the influence of the conduit inlet and outlet on the flow at $x \to \pm\infty$ is ignored because the channel length in our model is taken as infinite when compared with the channel height. The far-field flow is assumed to be unidimensional and fixed far from the origin with a constant volumetric flow throughout the channel. Moreover, the ionic strength is assumed high enough to justify the use of an infinitesimal EDL thickness relative to the channel height.

Derivation

Our solution was derived in four basic steps: First, we solved for the velocity and pressure distributions far away ($x \to \pm\infty$) from the origin at $x = 0$; we will refer to these expressions as the far-field solutions. Second, by subtracting out the upstream far-field solution, $x < 0$, over the entire domain, we ensure that the remaining solution goes to zero as $x \to -\infty$. Third, the remaining near-field problem is solved by utilizing the double-sided Laplace transformation.[25] Finally, the upstream far-field solution is added back to the resulting near-field solution in order to obtain a complete solution across the entire domain.

Far-Field Solution. Both the pressure gradient and the velocity lose their x-dependence far away from the origin, so the far-field equations of motion simplify to the ODEs

$$\frac{d^2V_{x\infty}^{\pm}}{dy^2} = \frac{K^{\pm}}{\eta} \tag{5}$$

where $K^{\pm}$ are the far-field pressure gradients. Applying boundary conditions given by Eq. 4, we find

$$V_{x\infty}^{\pm} = u^{\pm} + \frac{3}{2}(\langle V_x \rangle - u^{\pm})\left\{1 - \left(\frac{y}{H}\right)^2\right\} \tag{6}$$

where $\langle V_x \rangle$ is the mean velocity and Eq. 6 is identical to one presented by other researchers.[26] The stream functions associated with the far-field solutions can be found by integrating Eq. 6 with one more boundary condition, $\psi_{\infty}^{\pm} = 0$ at $y = H$ to obtain

$$\psi_{\infty}^{\pm} = \frac{y}{2}\langle V_x \rangle\left\{3 - \left(\frac{y}{H}\right)^2\right\} - \frac{y}{2}u^{\pm}\left\{1 - \left(\frac{y}{H}\right)^2\right\} - H\langle V_x \rangle. \tag{7}$$

The difference between the upstream and downstream far-field stream functions is

$$\delta\psi_{\infty} = \psi_{\infty}^{+} - \psi_{\infty}^{-} = \frac{y}{2}(u^{-} - u^{+})\left\{1 - \left(\frac{y}{H}\right)^2\right\}. \tag{8}$$

Similarly, the difference between the far-field pressures is

$$\delta P_{\infty} = (K^{+} - K^{-})x = \frac{3\eta}{H^2}(u^{+} - u^{-})x \tag{9}$$

and we will use these differences, Eqs. 8 and 9, later.

Near-Field Solution. After subtracting the upstream far-field stream function from the entire domain, the near-field stream function becomes

$$\vec{\Psi}^{*} \equiv \vec{\Psi} - \vec{\Psi}_{\infty}^{-} = \left[0,\ 0,\ \psi - \psi_{\infty}^{-}\right]^{T}, \tag{10}$$

with the governing equation

$$\Delta^2\psi^{*} = \nabla^4\psi^{*} = \frac{\partial^4\psi^{*}}{\partial x^4} + 2\frac{\partial^4\psi^{*}}{\partial x^2\partial y^2} + \frac{\partial^4\psi^{*}}{\partial y^4} = L^4(\psi^{*}) = L^2(L^2\psi^{*}) = 0 \tag{11}$$

and boundary conditions

$$V_y^{*}\Big|_{y=\pm H} = -\frac{\partial\psi^{*}}{\partial x}\Big|_{y=\pm H} = 0 \tag{12a}$$

$$V_x^{*+}\Big|_{y=\pm H} = \frac{\partial\psi^{*+}}{\partial y}\Big|_{y=\pm H} = -\frac{\varepsilon(\varsigma^{+} - \varsigma^{-})}{\eta}E \equiv u^{+} - u^{-} \tag{12b}$$

$$V_x^{*-}\Big|_{y=\pm H} = \frac{\partial\psi^{*-}}{\partial y}\Big|_{y=\pm H} = -\frac{\varepsilon(\varsigma^{-} - \varsigma^{-})}{\eta}E \equiv u^{-} - u^{-} = 0 \tag{12c}$$

It is convenient to use the unit (Heaviside) step function to combine Eqs.12b and 12c,

$$V_x^{*}|_{y=\pm H} = \frac{\partial\psi^{*}}{\partial y}\Big|_{y=\pm H} = (u^{+} - u^{-})\mathbf{H}(\mathrm{x}) \quad \text{where } \mathbf{H}(\mathrm{x}) = \begin{cases} 0 & x < 0 \\ 1 & x \geq 0 \end{cases}. \tag{12d}$$

The two-sided Laplace transform[25] is carried out by

$$\phi_{\psi}(s,y) \equiv \int_{-\infty}^{+\infty} \psi^{*}(x,y)e^{-sx}dx \tag{13}$$

which converts the biharmonic PDE Eq. 11 into a fourth-order ODE:

$$\frac{d^4\phi_{\psi}}{dy^4} + 2s^2\frac{d^2\phi_{\psi}}{dy^2} + s^4\phi_{\psi} = \left(\frac{d^2}{dy^2} + s^2\right)\left(\frac{d^2}{dy^2} + s^2\right)\phi_{\psi} = 0. \tag{14}$$

The boundary conditions are also transformed into Laplace space, accordingly. From Eqs. 12 and 13, we find

$$-s\,\phi_{\psi}\Big|_{y=\pm H} = 0, \tag{15a}$$

$$\frac{d\phi_{\psi}}{dy}\Big|_{y=\pm H} = \frac{u^{+} - u^{-}}{s}. \tag{15b}$$

The general solution of Eq. 14 is

$$\phi_{\psi}(s,y) = C_1\cos[sy] + C_2 y\cos[sy] + C_3\sin[sy] + C_4 y\sin[sy] \tag{16}$$

where the C_i are constants of integration which can be determined by using the four boundary conditions, Eqs. 15a and 15b. The solution to the problem in Laplace space is

$$\phi_{\psi}(s,y) = \frac{2(u^{+} - u^{-})(H\cos[Hs]\sin[sy] - y\sin[Hs]\cos[sy])}{s(2Hs - \sin[2Hs])} = \frac{N_{\psi}(s,y)}{D_{\psi}(s)} \tag{17}$$

where $N_{\psi}(s,y) \equiv 2(u^{+} - u^{-})(H\cos[Hs]\sin[sy] - y\sin[Hs]\cos[sy])/s^3$ and $D_{\psi}(s) \equiv (2Hs - \sin[2Hs])/s^2$ denote the numerator and denominator of the solution. The Heaviside expansion[27] is now used to invert the solution from Laplace space.

$$\psi^{*+} = \lim_{S\to 0}[s\phi_{\psi}(s,y)] + \sum_{\text{All } S_j<0} \frac{N_{\psi}(s_j,y)}{\frac{\partial}{\partial s}D_{\psi}(s)\big|_{s=s_j}}e^{s_j x} \quad \text{for } x > 0 \tag{18a}$$

$$\psi^{*-} = -\sum_{\text{All } S_j>0} \frac{N_{\psi}(s_j,y)}{\frac{\partial}{\partial s}D_{\psi}(s)\big|_{s=s_j}}e^{-s_j x} \quad \text{for } x < 0 \tag{18b}$$

where s_j are the roots of the characteristic equation, $D_{\psi}(s_j) = 0$ which has a simple root at $s = 0$.

Velocity and Pressure Distributions. The explicit analytical solution of the original stream function ($\vec{\Psi}$) is found by adding Eqs. 7 and 18, and the local velocity can be found by

differentiating the original stream function. Similarly, the near-field pressure in Laplace space has the general solution,

$$\phi_P(s,y) \equiv \int_{-\infty}^{+\infty} P^*(x,y)e^{-Sx}dx = C_5\cos[sy] + C_6\sin[sy], \quad (19)$$

where C_5 and C_6 are constants of integration, and $P^{*\pm} \equiv P^{\pm} - K^{-}x$. By relating pressure to the velocity using the Navier-Stokes equations, we find the near-field pressure distribution,

$$\phi_P(s,y) = \frac{4\eta(u^+ - u^-)(\sin[Hs]\cos[sy])}{2Hs - \sin[2Hs]} = \frac{N_P(s,y)}{D_P(s)} \quad (20)$$

where $N_P(s,y) \equiv 4\eta(u^+ - u^-)(\sin[Hs]\cos[sy])$ and $D_P(s) \equiv 2Hs - \sin[2Hs] = D_\psi(s)$. Note that the denominator of Eq. 20 is exactly the same as in Eq. 17. Thus, roots for the stream function coincide with those for the pressure because of the characteristics of the momentum equation. For inversion, the Heaviside expansion is again used to obtain

$$P^{*+} = x\lim_{S\to 0}\left[s^2\phi_P(s,y)\right] + \sum_{\text{All } S_j<0} \frac{N_P(s_j,y)}{\frac{\partial}{\partial s}D_P(s)\Big|_{s=s_j}} e^{s_j x} \quad \text{for } x > 0 \quad (21a)$$

$$P^{*-} = -\sum_{\text{All } S_j>0} \frac{N_P(s_j,y)}{\frac{\partial}{\partial s}D_P(s)\Big|_{s=s_j}} e^{-s_j x} \quad \text{for } x < 0 \quad (21b)$$

The downstream far-field pressure is then added to obtain the overall pressure distribution. The first 10 nondimensional roots ($\hat{s} \equiv Hs$), as determined by the Secant method in *Mathematica* using a maximum of 5000 iterations, are listed in Table 1.

Accuracy

Final Value Theorem. To check the accuracy of the inverse Laplace transformation, we apply the final value theorem to find the difference between the far-field stream functions from the Laplace transform when compared with the difference in the far-field solutions determined analytically, i.e., Eq. 8. The theorem states that

$$\lim_{x\to\infty}[\psi^*(x,y)] = \lim_{S\to 0}\left[s\phi_\psi(s,y)\right] = \frac{y}{2}(u^- - u^+)\left\{1 - \left(\frac{y}{H}\right)^2\right\} = \psi_\infty^+ - \psi_\infty^- \quad (22a)$$

$$\lim_{x\to\infty}[P^*(x,y)] = x\lim_{S\to 0}\left[s^2\phi_P(s,y)\right] = \frac{3\eta}{H^2}(u^+ - u^-)x = (K^+ - K^-)x, \quad (22b)$$

for which the results on the far right-hand side are identical to Eqs. 8 and 9, respectively. Eqs. 22a and 22b show that the first term in Eq. 18a and the first term in Eq. 21a are the difference between the upstream and downstream far-field stream functions and the difference between the upstream and downstream far-field pressures, respectively.

Convergence and Continuity at $x = 0$. Our analytical solutions are basically trigonometric Fourier series. When we try to reconstruct discontinuous functions with these series solutions, many terms are needed to avoid truncation errors and, in this case the solutions exhibit Gibbs ringing[28] near the discontinuity at $x = 0$. This problem is mitigated by using one of several available filters.[29] We multiplied a Lanczos Sigma factor,[30] $\sin(n\pi/(N+1))/(n\pi/(N+1))$, to the series solutions in order to reduce the Gibbs phenomenon. Here, n corresponds to the nth eigenfunction, and N is the number of roots used to express the finite series solutions.

While the ζ-potential changes discontinuously along the wall boundary, the streamfunction, velocity, and pressure should all display continuity at the junction across the channel from a physical point of view. Such continuity is closely approximated by increasing the number of eigenfunctions used in our series solutions. If only a few terms are considered, the solutions in upstream region ($x < 0$) and downstream region ($x \geq 0$) do not match at the interface ($x = 0$). On the other hand, as mentioned in the previous section, the infinite series converges very slowly near $x = 0$. We are now in a position to test continuity between the upstream and downstream variables at the junction by estimating the stream function differences, $\delta\psi = \psi^+ - \psi^-$. The filtering flattens out the wavy errors. By contrast, the filter swells the error near the wall boundary. By trading off between artificial errors caused by filtering near the wall and convergence time, we used up to 200 terms with filtering in this study. This allows both fast convergence and good matching at the junction. The maximum absolute error in discontinuity of the stream functions between upstream and downstream is ~0.1%.

Table 1. First 10 Roots for our Analytical Solutions Based on Characteristic Equation, $\hat{D}_\psi(\hat{s}_j) = \hat{D}_P(\hat{s}_j) = 2\hat{s}_j - \sin[2\hat{s}_j] = 0$

J	$\hat{s}_j < 0$	$\hat{s}_j > 0$
1	−3.748838138888 ± 1.384339141494*i*	3.748838138888 ± 1.384339141494*i*
2	−6.949979856988 ± 1.676104942427*i*	6.949979856988 ± 1.676104942427*i*
3	−10.119258853915a ± 1.858383839876*i*	10.119258853915 ± 1.858383839876*i*
4	−13.277273632746 ± 1.991570820170*i*	13.277273632746 ± 1.991570820170*i*
5	−16.429870502535 ± 2.096625735216*i*	16.429870502535 ± 2.096625735216*i*
6	−19.579408260032 ± 2.183397558835*i*	19.579408260032 ± 2.183397558835*i*
7	−22.727035732178 ± 2.257320224741*i*	22.727035732178 ± 2.257320224741*i*
8	−25.873384151411 ± 2.321713978526*i*	25.873384151411 ± 2.321713978526*i*
9	−29.018831029547 ± 2.378757559041*i*	29.018831029547 ± 2.378757559041*i*
10	−32.163616856643 ± 2.429958323949*i*	32.163616856643 ± 2.429958323949*i*

Other surface velocity distributions

In the analytical solution represented by Eq. 18, a discontinuity in the surface velocity was introduced at $x = 0$ which is also the interface between the upstream, $x > 0$, and downstream, $x < 0$, sections of the channel. This produces a "clean" solution, in the sense that it contains the fewest number of adjustable parameters, but at the same time this "simplest" approach does not provide an obvious way to extrapolate this technique to more complex surface boundary conditions. In fact, the two-sided Laplace transform presented here can readily handle velocity distributions of arbitrary complexity, including multiple step discontinuities, pulse and impulse distributions, or other stepwise continuous functions, i.e.,

$$V^- = f^-(x) + u^-; \quad x < 0 \tag{23a}$$

$$V^+ = f^+(x) + u^+; \quad x > 0 \tag{23b}$$

as long as their Laplace transforms exist. The main difficulty that arises in this case is that the far-field solutions cannot necessarily be subtracted out unless the far-field velocities are constant, i.e., $\lim_{x\to\pm\infty}\left[f^{\pm}(x)\right] \to 0$. However, in this case, Eq. 12d becomes

$$V_x^*\Big|_{y=\pm H} = \frac{\partial \psi^*}{\partial y}\Big|_{y=\pm H} = (u^+ - u^-)\mathbf{H}(x) + f^+(x)\mathbf{H}(x) + f^-(x)\mathbf{H}(-x) \tag{24}$$

and, in the special case where a pair of step discontinuities with an intermediate velocity, u^i, between $x = 0$ and $x = a$, this formula can be expressed as

$$V_x^*\Big|_{y=\pm H} = \frac{\partial \psi^*}{\partial y}\Big|_{y=\pm H} = (u^+ - u^i)\mathbf{H}(x-a) + (u^i - u^-)\mathbf{H}(x) \tag{25}$$

where the jump at $x = 0$ can be removed by eliminating the last term on the right. Finally note that the two boundary conditions do not have to be symmetric.

Discussion of Results

This section consists of three parts. Part 1 illustrates the properties of the roots corresponding to the eigenfunctions in the series solutions. Part 2 focuses on recirculation and separation of the flow, Taylor dispersion, and band broadening effects. In Part 3, we discuss the overall dispersion in microchannel under different conditions. All the results displayed here are arrived at under the consideration of using buffered water within a 5-μm height microchannel (i.e. $\eta = 1.25 \times 10^{-3}$ kg/(m s) and $H = 2.5 \times 10^{-6}$ m), although the solution to the biharmonic equation is expected to apply under a wide variety of fluids and in microchannels of different geometrical proportions.

Base solution

From Table 1 it is obvious that all of the roots are complex and that the roots appear in conjugate sets of four. In other words, if $\hat{s_i}$ is an eigenvalue, so are $-\hat{s_i}$ as well as the complex conjugates of both $\hat{s_i}$ and $-\hat{s_i}$. Care must be taken to ensure that $\hat{s} = 0$ is not a repeated root and that there are no nonzero repeated eigenvalues. The real parts of the roots increase approximately by $(n + 1/4)\pi$ for large n while the corresponding positive imaginary parts increase much more slowly. Importantly, the near-field solutions given by Eqs. 18 and 21 decay exponentially to zero in both axial direction, where the real part of each root is a spatial decay parameter. The real part of the leading eigenvalue ($\mathrm{Re}[\hat{s_1}] \cong \pm 3.745$ as shown in Table 1) is the most significant number among all roots since the first decay parameter, i.e. principal eigenvalue, determines the extent of the region over which the near-field terms vanish. The search for complex roots is typically executed by using numerical techniques such as Newton's method and Secant method for higher accuracy. Although we show the eigenvalues to 12 digits to the right of the decimal point in Table 1, all the calculations are actually done with higher precision numbers (at least 20 digits) by using the *Mathematica*® command option: "AccuracyGoal $\geq$ 20, PrecisionGoal $\to$ 20, WorkingPrecision $\to$ 50, MaxIterations $\to$ 5000."

Flow results and their implications

In this section, we present the flow patterns in planar microchannels for nonuniform zeta potential cases. In many electrophoretic separation processes, EOF is used to mobilize the sample bands. Uniform (ideal) EOF is especially useful for this kind of applications. However, the focus band will undergo significant changes in shape if the flow pattern is not plug-like. Here we discuss the effects of resulting flow distribution on sample band's shape originated from the nonuniform zeta potential.

Figure 2 illustrates the behavior of the streamlines under the condition where there is a sudden change in ζ-potential

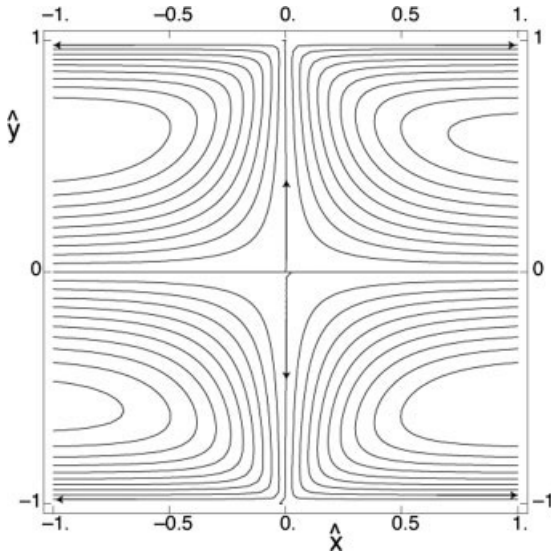

Figure 2. Streamlines for step change in ζ-potential along the wall ($\hat{y} = \pm 1$) for $u^+ = 1.0$ mm/s, $u^- = -u^+$, and $\langle V_x \rangle = 0$.

In this figure both x and y are normalized as $\hat{x} \equiv x/H$ and $\hat{y} = y/H$.

at $x = 0$. Here the special case, symmetric EOF velocity ($u^+ = -u^-$) with no flow rate, $\langle V_x \rangle = 0$ (i.e. $K^{\pm} = \frac{3\eta}{H^2} u^{\pm}$), is considered. The slip velocity at the wall is utilized and its value is assumed to be constant at 1 mm/s (e.g., $\varepsilon = 6.95 \times 10^{-10}$ F/m, $\zeta^+ = -35.2$ mV, $\eta = 1.025 \times 10^{-3}$ Pa s, $E = 419$ V/cm). For this case, if a sample is located in the far-field region, its shape will skew like the shape of a "crescent" because the flow around the center of the channel is in the opposite direction to the flow in the region close to the wall.

Figure 3 shows the dependence of a nonzero mean velocity on the streamlines. The symmetrical step change condition, $u^+ = -u^-$, is maintained to observe how the bulk velocity affects flow patterns. In Figure 3a, $\langle V_x \rangle = 0.1u^+$ is applied; some of the fluid travels in the downstream direction, especially at the center of the upstream channel. Thus the intersection is shifted downstream. The more the flow rate is increased, the more fluid is transported in the downstream direction. This interaction will eventually vanish as the volumetric flow rate is increased and most of the fluid will head downstream as shown in Figure 3b. Consequently, the higher mean velocity moderates the effects of the surface discontinuity. Because of the fact that u^- is negative, a reverse flow occurs near the wall boundary at the junction even if a relatively high flow rate is applied. In Figure 3c, almost all streamlines are situated parallel to each other in the far-field region of the downstream side. If this flow is used to mobilize a sample band, there should not be any distortion of the sample in the region where longitudinal location, x, is equal to or greater than one characteristic length, H, namely $\hat{x} \geq 1$ according to Figure 3c.

We must point out that changing the mean velocity requires consideration of band broadening effects and Taylor dispersion. In bioanalytical separation, the theoretical plate height can be presented as[31]

$$\text{HETP} = A + B\frac{1}{\langle V_x \rangle} + C\langle V_x \rangle \tag{23}$$

where HETP is the theoretical plate height, A, B, and C are constants for a particular system. The first term indicates eddy diffusion, which is simply a constant. The B- and C-terms in the van Deemter equation represent contributions to band broadening because of the longitudinal diffusion and resistance to mass transfer. Both the second and third terms depend on the mean velocity, $\langle V_x \rangle$. Originally, Eq. 23 was introduced for gas chromatography,[31] but the equation applies for liquid chromatography as well. In the case of microchannel electrophoresis in a straight channel, eddy diffusion can be ignored since the carrier fluid is a uniformly-filled single phase liquid. Nevertheless, as long as the second and third terms exist, attention needs to be paid at finite values of $\langle V_x \rangle$.

It is well documented that Taylor dispersion causes band broadening because the velocity profile across the channel is not plug-like in mixed electroosmotic and pressure driven flows. The effective dispersion coefficient for Poiseuille flow in a tube is $D + \langle V_x \rangle^2 r^2/(48D)$[32] where D is the molecular diffusivity and r is the tube radius, while in the case of two parallel plates the coefficient[33] is $D + 2\langle V_x \rangle^2 H^2/(105D)$.

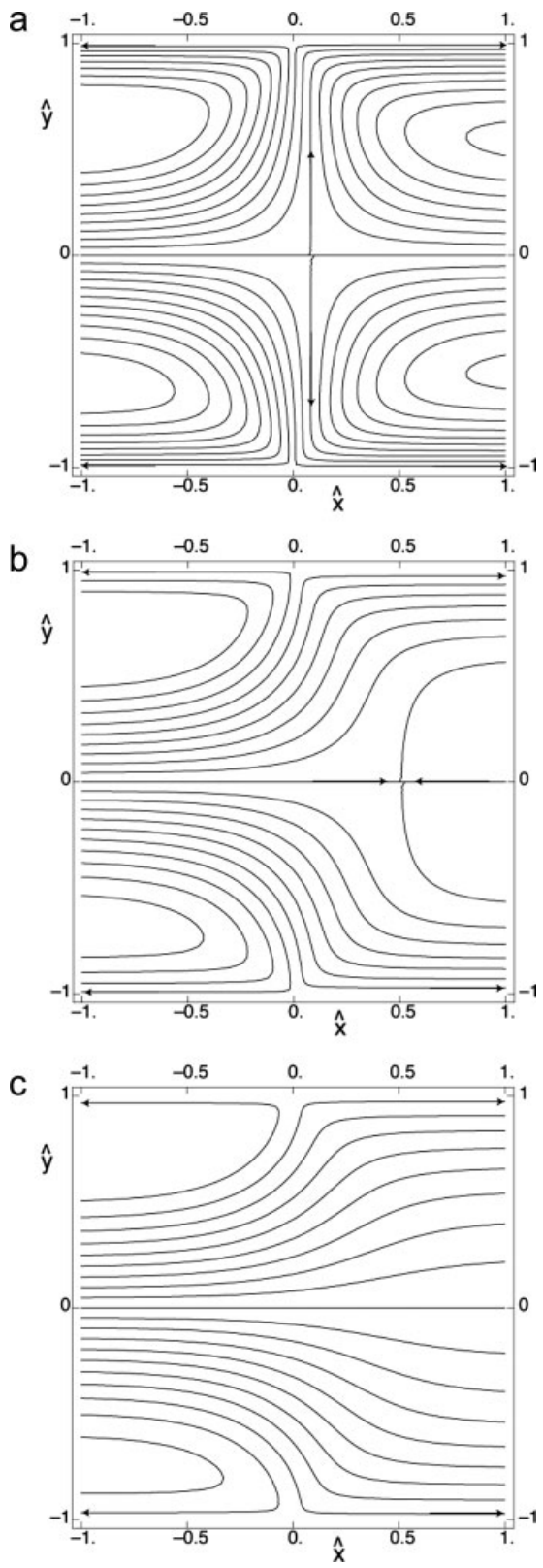

Figure 3. Influence of the mean velocity on the streamlines for (a) $\langle V_x \rangle = 0.1u^+$, (b) $\langle V_x \rangle = 0.5u^+$, and (c) $\langle V_x \rangle = 0.1u^+$.

Here a symmetrical step change in ζ-potential is maintained (e.g. $u^+ = 1.0$ mm/s and $u^- = -u^+$).

Beard's work draws attention to the treatment of the mean velocity in our study where, indeed, longitudinal dispersion for velocity distribution presented in Figure 3c is higher than that of Figure 3a.

In the case where there is no axial pressure gradient at the downstream region ($x > 0$) the normalized velocity vectors $\left(\hat{V}_x, \hat{V}_y\right)$ are shown in Figure 4 for an average velocity of 1 mm/s. Here no pressure gradient means that the flow was driven only under the action of the EK body force. This case is important when either the axial velocity is low, or when the height of the channel is small because convective-dispersion of sample is desired to be small. For a symmetric change in zeta potential at the interface, some of the fluid travels in the upstream direction (Figure 4a), especially very close to the wall. This local reverse flow results in circulation near the wall so that at the upstream region the sample shape may be a "crescent." There is finite value of the velocity in $\hat{y}$ direction around the interface ($x = 0$), but not in far-field ($x \to \infty$). Thus, the "crescent" shape remains almost the same in downstream region.

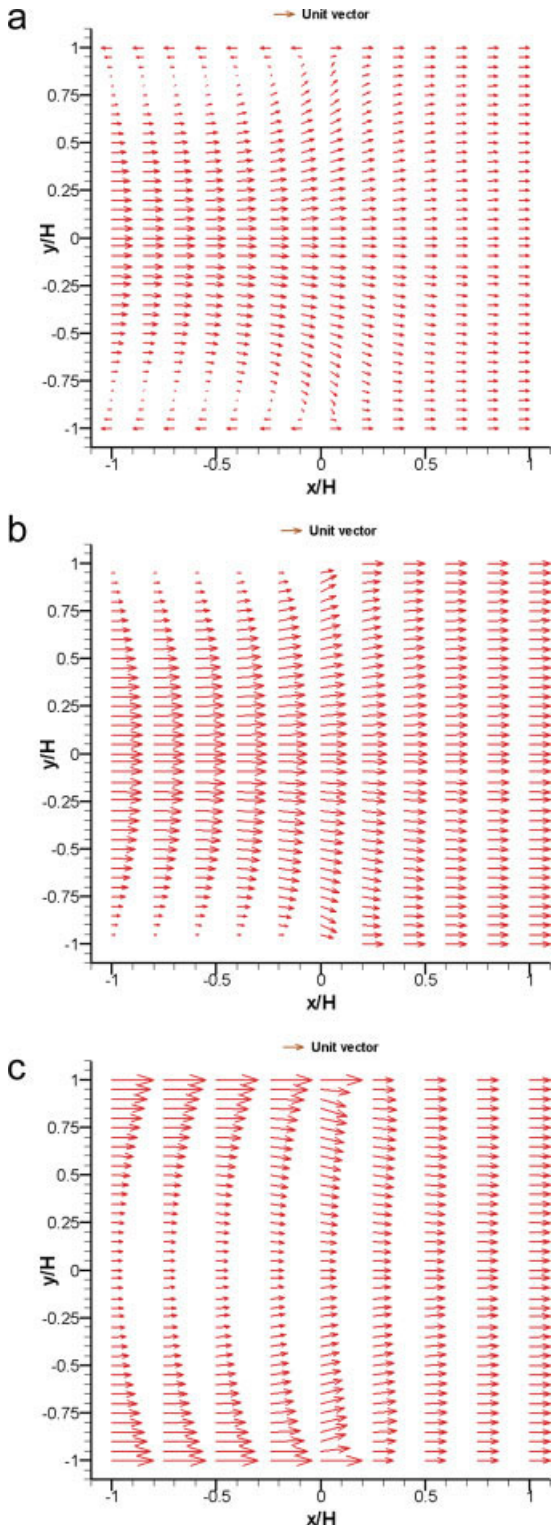

Figure 4b depicts the case for which the driving mechanism of the flow is changed from pure pressure driven flow in upstream region ($u^- = 0$) to pure EOF in downstream region ($u^+ = \langle V_x \rangle$). This case is similar to the experimental work of Herr et al.[16] One can achieve this type of channel surface by selective patterning/coating of the surface. In this case, the band deformation is relatively small compared to the case presented in Figure 4a as there is no circulation. In addition to that, since the magnitude of the velocity in $\hat{y}$ direction is smaller than that in Figure 4a, the concentration of sample at the center of the channel will be a bit higher. Figure 4c introduces the case when the slip velocity is bigger in the upstream region than that in the downstream region ($u^- > u^+$). The main difference in flow pattern between Figure 4c and Figures 4a,b is the direction of velocity along the $\hat{y}$ axis. Based on mass conservation, the vectors near the interface ($\hat{x} = 0$) direct toward the center of the channel in Figure 4c whereas the vectors at the same location face toward the wall in Figures 4a,b. This leads to the observation of higher concentration of sample at the center of the channel when $u^- > u^+$.

We next readjust the mean velocity back to zero and separately vary the EOF velocities (or ζ-potentials) upstream, u^-, and downstream, u^+. Figure 5 depicts the streamlines for (a) $u^- = 0$, (b) $u^- = -0.5u^+$, and (c) $u^- = +0.5u^+$, where $u^+ = 1.0$ mm/s. Based on the streamline presented in Figure 5a, a "crescent" shape sample band will probably form on the downstream side for case-a ($u^- = 0$). Since there is almost no velocity component in the upstream region, the bandwidth is not affected by the flow until it reaches the downstream area. Figures 5b,c show a similar trend in the far-field region of the downstream side, yet they exhibit different flow profiles as they approach the interface between the upstream and downstream regions. The sample may take on a "semicurcular" shape near the junction in Figure 5b for $u^- = -0.5u^+$. On

Figure 4. The normalized velocity vectors for no pressure gradient flows with step change in ζ-potential along the wall ($\hat{y} = \pm 1$).

Case (a) $\langle V_x \rangle = 1$ [mm/sec], $u^+ = \langle V_x \rangle$, $u^- = -\langle V_x \rangle$; (b) $\langle V_x \rangle = 1$ mm/sec, $u^+ = \langle V_x \rangle$, $u^- = 0$; and (c) $\langle V_x \rangle = 1$ mm/sec, $u^+ = \langle V_x \rangle$, $u^- = 2\langle V_x \rangle$. The velocity components V_x and V_y are normalized by $|u^+ - u^-|$. The length of a normalized unit vector is shown in each panel. [Color figure can be viewed in the online issue, which is available at www.interscience.wiley.com.]

the other hand, for $u^- = 0.5u^+$, a shape between a "crescent" and a "trapezoid" may be obtained near the junction as shown in Figure 5c.

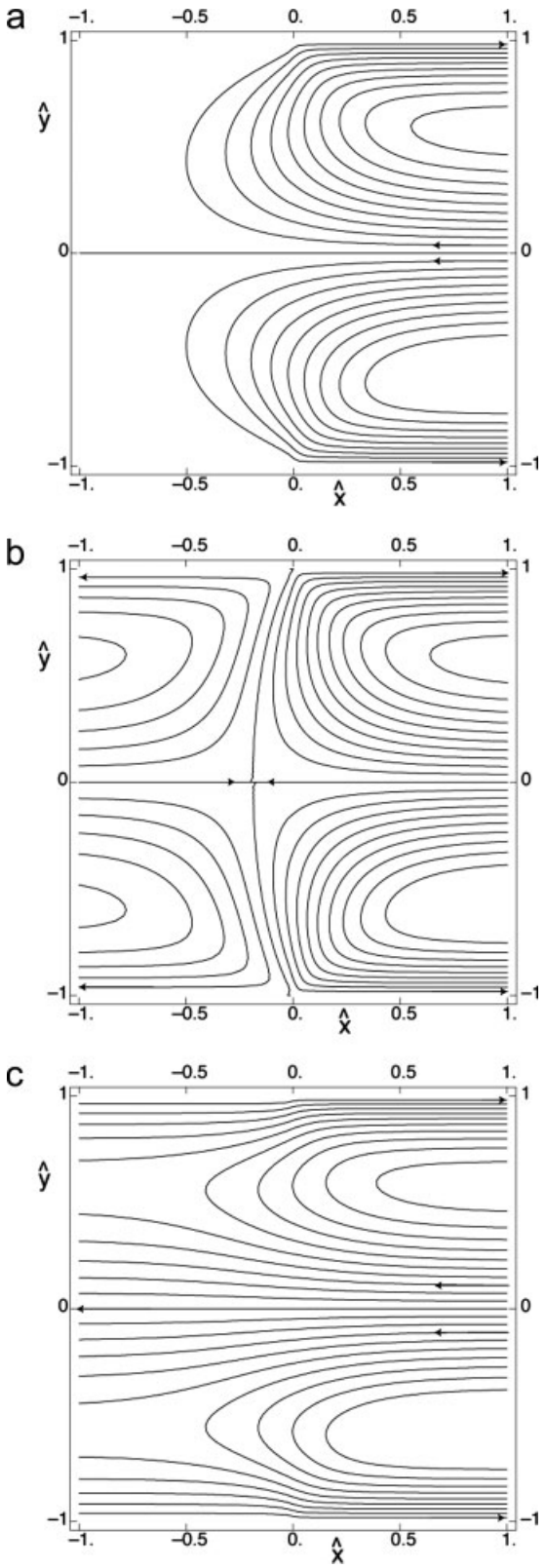

The pressure gradient is also important in the prediction of sample dispersion. We present nondimensional pressure distribution ($\hat{P}^{\pm} \equiv P^{\pm}/\{(u^+ - u^-)\eta/H\}$) in Figure 6. The pressure distribution presented in Figure 6a corresponds to the velocity distribution presented in Figure 2 ($u^- = -u^+$ and $\langle V_x \rangle = 0$). The pressure distributions for other conditions are also shown in Figure 6b ($u^- = 0$ and $\langle V_x \rangle = 0$) and Figure 6c ($u^- = 0$ and $\langle V_x \rangle = 1.0u^+$) for $u^+ = 1.0$ mm/s. Except for the special condition ($u^- = -u^+$ and $\langle V_x \rangle = 0$) in Figure 6a, Figures 6b,c indicate bulk flow direction by induced pressure gradient. In Figures 6a–c, holes near the wall on the interface between upstream and downstream indicate that there are flows toward these holes. This suggests that the velocity in cross-stream direction cannot be ignored in contrast to the hypothesis made by Ren and Li.[34] This is why band distortion happens especially near the wall where the discontinuous ζ-potential is applied.

The normalized, streamwise velocity component, $\hat{V}_x$ ($\equiv V_x/|u^+ - u^-|$) is presented in Figure 7 for the same flow parameters used in Figure 6 and is repeated for the nondimensional cross-stream component, $\hat{V}_y$, in Figure 8. From these we can see how the velocity develops under the step ζ-potential boundary condition. The parabolic velocity profiles in Figures 7a,c suggest the existence of a pressure gradient which corresponds to the pressure distribution in Figure 6. In other words, there is no axial velocity in upstream region in the case of Figure 7b as expected from Figure 6b. Moreover, the maximum velocity coincides with the magnitude of the mean velocity. On the other hand, it is evident that the velocity in y-direction occurs surrounding the junction for all cases as shown in Figure 8.

Overall dispersion

It turns out that, for zone electrophoresis where solutes electromigrate at a constant velocity that is proportional to the electric field, most of the dispersion that occurs in a long slit with discontinuous surface velocities happens outside the neighborhood of the velocity jump. The most important effect of the discontinuity is not dispersion near the disturbance, but the fact that the discontinuity in surface velocities must give rise to a parabolic flow in either the upstream or downstream or both sections of the channel and it is the parabolic portion of these flows which gives rise to Taylor dispersion.

As noted in the solution, and particularly in the smallest positive and negative eigenvalues, the jump disturbance occupies less than one slit width upstream and downstream of the discontinuity. Since most capillaries and microchips used for zone electrophoresis have aspect ratios, length-to-

Figure 5. Influence of the relationship between the upstream EOF velocity (u^-) and the downstream EOF velocity (u^+) on the streamlines for (a) $u^- = 0$, (b) $u^- = -0.5u^+$, and (c) $u^- = +0.5u^+$.

Here, the volumetric flow rate is zero, i.e., $\langle V_x \rangle = 0$, and $u^+ = 1.0$ mm/s. Slight changes in the relationship between u^- and u^+ significantly affect the flow pattern and the sample shape.

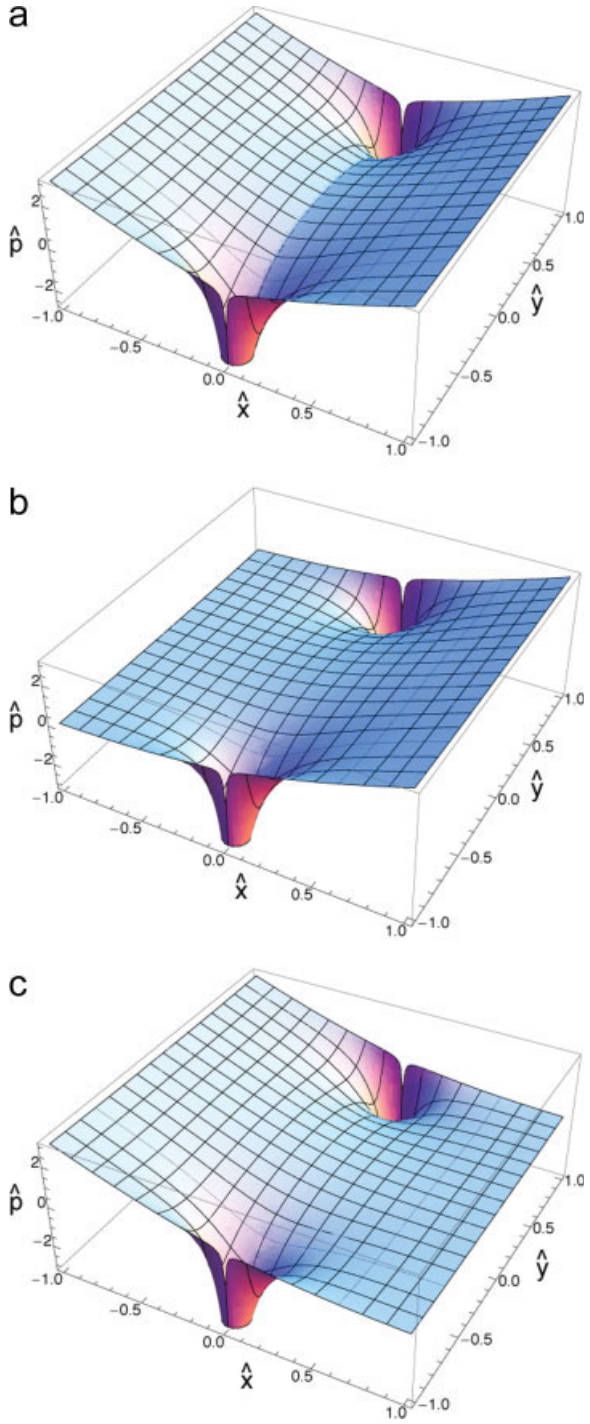

Figure 6. The pressure distribution due to a step change in the ζ-potential along the wall ($\hat{y} = \pm 1$) for (a) $u^- = -u^+$ and $\langle V_x \rangle = 0$, (b) $u^- = 0$ and $\langle V_x \rangle = 0$, (c) $u^- = 0$ and $\langle V_x \rangle = 1.0u^+$.

Here $u^+ = 1.0$ mm/s. Singularities near the wall in the neighborhood of the origin ($\hat{x} = 0$, $\hat{y} \approx \pm 1$) are indicative of recirculating flows. [Color figure can be viewed in the online issue, which is available at www.interscience.wiley.com.]

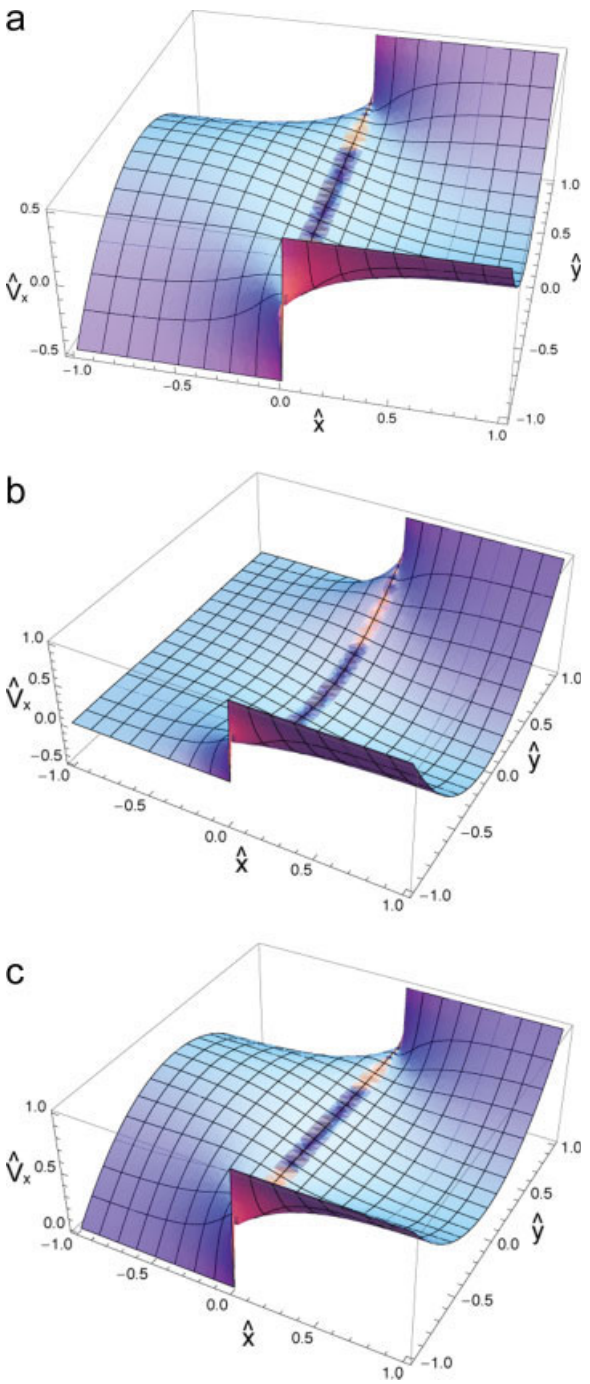

Figure 7. The nondimensional streamwise velocity distribution that occurs near a step change in ζ-potential along the wall ($\hat{y} = \pm 1$) for (a) $u^- = -u^+$ and $\langle V_x \rangle = 0$, (b) $u^- = 0$ and $\langle V_x = 0 \rangle$, (c) $u^- = 0$ and $\langle V_x \rangle = 1.0u^+$ where $u^+ = 1.0$ mm/s.

There is no axial velocity in the upstream region in case b. The other cases show a parabolic velocity profile. [Color figure can be viewed in the online issue, which is available at www.interscience.wiley.com.]

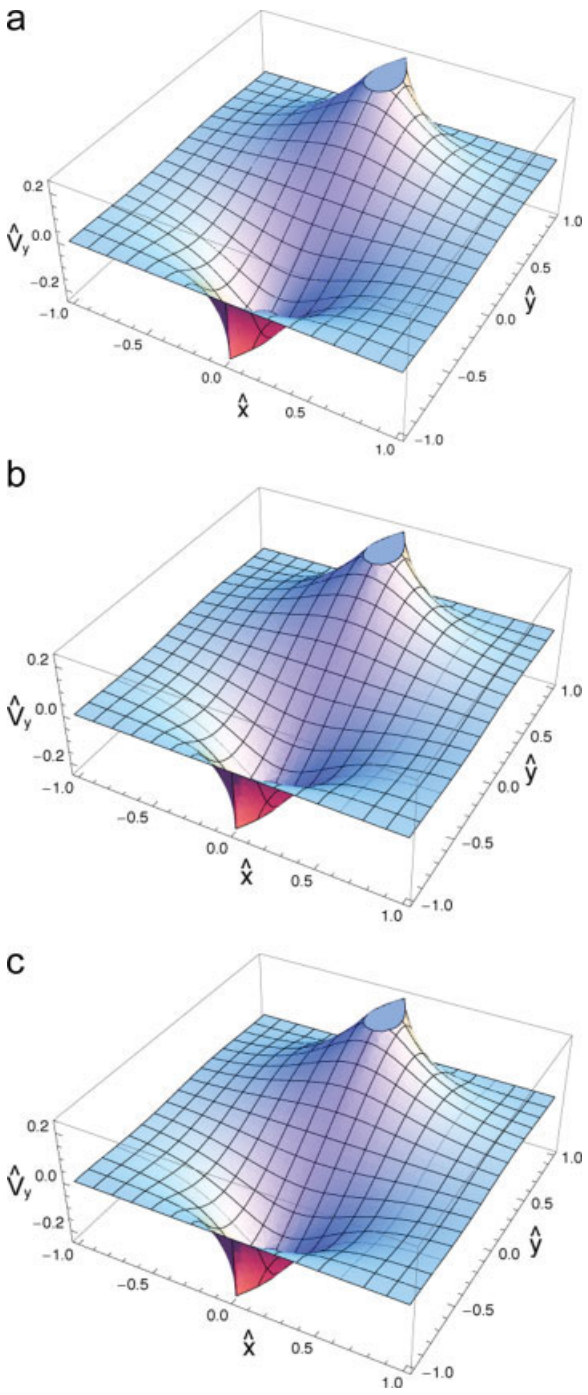

Figure 8. The nondimensional cross-stream velocity distribution in the neighborhood of a step change in ζ-potential along the wall ($\hat{y} = \pm 1$) for (a) $u^- = -u^+$ and $\langle V_x \rangle = 0$, (b) $u^- = 0$ and $\langle V_x \rangle = 0$, (c) $u^- = 0$ and $\langle V_x \rangle = 1.0u^+$ where $u^+ = 1.0$ mm/s.

The location of the cusps near the wall at the interface ($\hat{x} = 0$, $\hat{y} \approx \pm 1$) coincide with those in Figure 6. [Color figure can be viewed in the online issue, which is available at www.interscience.wiley.com.]

width, substantially greater than 100, even if the flow driven by the discontinuity were to completely mix the peaks over the length of the upstream and downstream disturbances, about 2H, it would still contribute minimally to dispersive spreading of the peak.

The main source of dispersion in these slits is due to the parabolic component in the far-field flows in the long runs upstream and downstream of the disturbance. The effect of these flows on dispersion can be guesstimated by superimposing Aris-Taylor dispersion theory on the parabolic components of the far-field flows. This concept is articulated in Eq. 26

$$D_{cO} = D_m + \frac{3\left(L^-\left(\langle V_x \rangle - u^-\right)^2 + L^+\left(\langle V_x \rangle - u^+\right)^2\right)H^2}{70\left(L^- + L^+\right)D_m} + \frac{\left(\langle V_x \rangle + u_m\right)H^2}{24\left(L^- + L^+\right)} \quad (26)$$

as a rough guide to dispersion in slits where u_m is the electrophoretic velocity of the solute undergoing dispersion, D_{cO} is the overall dispersion, D_m is the bulk diffusion coefficient, L^- is the length of the upstream channel, and L^+ is the length of the downstream channel. However, the reader is warned that accurate estimates of dispersion can only come from transient simulations which include both the far-field terms and the jump disturbance in the flow.

For the case where $L^- = L^+ = L$, the ratio of the third term in Eq. 26 to the second is

$$\text{ratio} = \frac{(u^- + u^+ + 2u_m)D_m}{(u^+ - u^-)^2 L} \ll 1 \quad (27)$$

There are two classes of exceptions to this formula. The first is in the instance of very short channels, which can roughly be characterized as occurring when the ratio in Eq. 27 approaches 1. This can easily occur in membrane pores and in microchip "vias." The second may happen in the case where solute stops within the jump disturbance flow. This cannot occur in zone electrophoresis, which is linear, but may take place with nonlinear methods like isotachophoresis and isoelectric focusing which can both place solutes at fixed points in a stationary steady-state. In fact, this situation probably does occur with isoelectric focusing in channels with silanols or other dissociable ionic groups.

The authors are not aware of any practical applications where a sharp discontinuity of this sort appears, it would correspond to butting two different capillaries together,[35] but with the increasing use of dissimilar materials and surface patterning in microchips, it is only a matter of time before functional step discontinuities are engineered into channels.

Conclusions

This work presents a solution to the biharmonic equation on a doubly-infinite domain using the double-sided Laplace transformation. Explicit mathematical expressions are presented for the streamfunction, the velocity, and the induced-pressure inside a straight microchannel with a step change in

ζ-potential near the x-axis origin. In practice, this step change in ζ-potential may occur when a surface is patterned or otherwise modified or when conduits made from two different materials are spliced together.

Filtering techniques, particularly the Lanczos sigma factor and the Cesàro mean filter, applied to a Fourier series dramatically reduce Gibbs ringing, so including up to 200 terms in the slowly converging series solution provides an accurate result with a reasonable convergence speed. Indeed, the test of continuity at the step-junction provides one measure of the accuracy of our results.

By examining plots of the analytical solution, one can see how the variation in flow near the discontinuity contributes to hydrodynamic dispersion, band broadening, flow separation, and recirculation. If the ζ-potential is discontinuously changed, a distortion of a sample band due to the flow may yield a variety of sample shapes including biconvex, biconcave, trapezoid, rectangle, half moon, and crescents which face either left or right. This analytical solution also indicates that the mean velocity influences band broadening and Taylor dispersion. Moreover, the pressure distributions and velocity distributions predicted by our analytical solution suggest that the transverse velocity component cannot be ignored, especially near the wall where the discontinuous ζ-potential is applied.

Acknowledgment

This material is based upon work partially supported by NSF grant No. CTS-0300802.

Notation

D = molecular diffusivity
D_P = denominator (characteristic equation) of ϕ_P
D_ψ = denominator (characteristic equation) of ϕ_ψ
$\vec{E}$ = applied electric field
E = electric field component in the streamwise direction
H = half channel height
$\mathbf{H}_{()}$ = Heaviside function
HETP = theoretical plate height
K = pressure gradient in far field
L = channel length
N_P = numerator of ϕ_P
N_ψ = numerator of ϕ_ψ
P = Pressure
s = roots of characteristic equation
u = Helmholtz-Smoluchowski slip velocity at the wall
u^1 = intermediate velocity
u_m = electrophoretic velocity
$\vec{V}$ = velocity field
V_x = velocity component in the streamwise direction
V_y = velocity component in the cross-stream direction
$\langle V_x \rangle$ = mean velocity
$\hat{x}$ = nondimensional x
$\hat{y}$ = nondimensional y

Greek letters

ε = dielectric constant
ϕ_P = near-field pressure in Laplace space
ϕ_ψ = near-field stream function in Laplace space
η = dynamic viscosity
μ_{eo} = electroosmotic mobility
Ω = vorticity
Ψ = Stream function
$\vec{\Psi}$ = Stream function vector
ζ = zeta potential

Subscripts

"max" = maximum value

Superscripts

"*" = near-field solutions
"$-$" = variables at upstream ($x < 0$)
"$+$" = variables at downstream ($x \geq 0$)

Symbols

"^" = nondimensional solutions for discontinuous zeta potential variation
"$\sim$" = nondimensional solutions for continuous zeta potential variation

Literature Cited

1. Hau WLW, Trau DW, Sucher NJ, Wong M, Zohar Y. Surface-chemistry technology for microfluidics. *J Micromech Microeng*. 2003;13:272–278.
2. Markstrom M, Cole KD, Akerman B. DNA electrophoresis in gellan gels. The effect of electroosmosis and polymer additives. *J Phys Chem B*. 2002;106:2349–2356.
3. Loughran M, Tsai SW, Yokoyama K, Karube I. Simultaneous isoelectric focusing of proteins in a micro-fabricated capillary coated with hydrophobic and hydrophilic plasma polymerized films. *Curr Appl Phys*. 2003;3:495–499.
4. Maeso N, Cifuentes A, Barbas C. Large-volume sample stacking-capillary electrophoresis used for the determination of 3-nitrotyrosine in rat urine. *J Chromatogr B Anal Technol Biomed Life Sci*. 2004;809:147–152.
5. Simal-Gandara J. The place of capillary electrochromatography among separation techniques—a review. *Crit Rev Anal Chem*. 2004;34:85–94.
6. Jo BH, Lerberghe LMV, Motsegood KM, Beebe DJ. Three-dimensional micro-channel fabrication in polydimethylsiloxane (PDMS) elastomer. *J Microelectromech Syst*. 2000;9:76–81.
7. Ma H, Davis RH, Bowman CN. A novel sequential photoinduced living graft polymerization. *Macromolecules*. 2000;33:331–335.
8. Lambert WJ, Middleton DL. pH hysteresis effect with silica capillaries in capillary zone electrophoresis. *Anal Chem*. 1990;62:1585–1587.
9. Towns JK, Regnier FE. Capillary electrophoretic separations of proteins using nonionic surfactant coatings. *Anal Chem*. 1991;63:1126–1132.
10. Ocvirk G, Munroe M, Tang T, Oleschuk R, Westra K, Harrison DJ. Electrokinetic control of fluid flow in native poly(dimethylsiloxane) capillary electrophoresis devices. *Electrophoresis*. 2000;21:107–115.
11. Anderson JL, Idol WK. Electroosmosis through pores with nonuniformly charged walls. *Chem Eng Commun*. 1985;38:93–106.
12. Adjari A. Generation of transverse fluid currents and forces by an electric field: electro-osmosis on charge-modulated and undulated surfaces. *Phys Rev E*. 1996;53:4996–5005.
13. Long D, Stone HA, Ajdari A. Electroosmotic flows created by surface defects in capillary electrophoresis. *J Colloid Interface Sci*. 1999;212:338–349.
14. Stroock AD, Weck M, Chiu DT, Huck WTS, Kenis PJA, Ismagilov RF, Whitesides GM. Patterning electro-osmotic flow with patterned surface charge. *Phys Rev Lett*. 2000;84:3314–3317.
15. Qian S, Bau HH. A chaotic electroosmotic stirrer. *Anal Chem*. 2002;74:3616–3625.
16. Herr AE, Molho JI, Santiago JG, Mungal MG, Kenny TW. Electroosmotic capillary flow with nonuniform zeta potential. *Anal Chem*. 2000;72:1053–1057.
17. Dutta P, Beskok A, Warburton TC. Numerical simulation of mixed electroosmotic/pressure driven microflows. *Numer Heat Transfer Part A*. 2002;41:131–148.

18. Brotherton CM, Davis RH. Electroosmotic flow in channels with step changes in zeta potential and cross section. *J Colloid Interface Sci*. 2004;270:242–246.
19. Potocek B, Gas B, Kenndler E, Stedry M. Electroosmosis in capillary zone electrophoresis with non-uniform zeta-potential. *J Chromatogr A*. 1995;709:51–62.
20. Erickson D, Li D. Influence of surface heterogeneity on electrokinetically driven microfluidic mixing. *Langmuir*. 2002;18:1883–1892.
21. Erickson D, Li D. Three dimensional structure of electroosmotic flows over periodically heterogeneous surface patterns. *J Phys Chem B*. 2003;107:12212–12220.
22. Hlushkou D, Kandhai D, Tallarek U. Coupled lattice-bolzmann and finite-difference simulation of electroosmosis in microfluidic channels. *Int J Numer Methods Fluids*. 2004;46:507–532.
23. Tian F, Li B, Kwok DY. Tradeoff between mixing and transport for electroosmotic flow in heterogeneous microchannels with nonuniform surface potentials. *Langmuir*. 2005;21:1126–1131.
24. Panton RL. *Incompressible Flow*, 2nd ed. New York: Wiley, 1996.
25. van Der Pol B, Bremmer H. *Operational Calculus Based on the Two-Sided Laplace Integral*, 2nd ed. London/New York: Cambridge University Press, 1955.
26. Dutta P, Beskok A. Analytical solution of combined electroosmotic/pressure driven flows in two-dimensional straight channels: finite Debye layer effects. *Anal Chem*. 2001;73:1979–1986.
27. Churchill RV. *Operational Mathematics*, 2nd ed. New York: McGraw-Hill, 1958.
28. Arfken G. *Mathematical Methods for Physicists*, 3rd ed. Orlando, FL: Academic Press, 1985.
29. Gottlieb D, Shu CW. On the Gibbs phenomenon and its resolution. *SIAM Rev*. 1997;39:644–668.
30. Hamming RW. *Numerical Methods for Scientists and Engineers*, 2nd ed. New York: Dover, 1986.
31. van Deemter JJ, Zuiderweg FJ, Klinkenberg A. Longitudinal diffusion and resistance to mass transfer as causes of nonideality in chromatography. *Chem Eng Sci*. 1956;5:272–289.
32. Guell DC, Cox RG, Brenner H. Taylor dispersion in conduits of large aspect ratio. *Chem Eng Commun*. 1987;58:231–244.
33. Beard DA. Taylor dispersion of a solute in a microfluidic channel. *J Appl Phys*. 2001;89:4667–4669.
34. Ren L, Li D. Electroosmotic flow in heterogeneous microchannels. *J Colloid Interface Sci*. 2001;243:255–261.
35. Michels DA, Hu S, Dambrowitz KA, Eggertson MJ, Lauterbach K, Dovichi NJ. Capillary sieving electrophoresis-micellar electrokinetic chromatography fully automated two-dimensional capillary electrophoresis analysis of *Deinococcus radiodurans* protein homogenate. *Electrophoresis*. 2004;25:3098–3105.

Manuscript received Dec. 12, 2006, and revision received Jun. 5, 2007.